ACS APPLIED MATERIALS & INTERFACES

Research Article

Cite This: ACS Appl. Mater. Interfaces XXXX, XXX, XXX−XXX

www.acsami.org

Visualizing Morphogenesis through Instability Formation in 4-D Printing

Dong Wu,[†,§] Jiaqi Song,[†,§] Zirui Zhai,[‡] Mutian Hua,[†] Cheolgyu Kim,[†] Imri Frenkel,[†] Hanqing Jiang,[‡] and Ximin He*[,†]

[†]Department of Materials Science and Engineering, University of California, Los Angeles (UCLA), Los Angeles, California 90095, United States

[‡]School for Engineering of Matter, Transport and Energy, Arizona State University, Tempe, Arizona 85281, United States

Supporting Information

ABSTRACT: Heterogeneous growth in a myriad of biological systems can lead to the formation of distinct morphologies during the maturation processes of different species. We demonstrate that the distinct circumferential buckling observed in pumpkins can be reproduced by a core−shell barrel structure using four-dimensional (4D) printing, taking advantage of digital light processing (DLP)-based three-dimensional (3D) printing and stimulus-responsive hydrogels. The mechanical mismatch between the stiff core and compliant shell results in buckling instability on the surface. The initiation and development of the buckling are governed by the ratio of core/shell radius, the ratio of core/shell swelling ratios, and the mismatch between the core and shell in stiffness. Furthermore, the rigid core not only acts as a source of circumferential confinement but also sets a boundary at the poles of the entire structure. The heterogeneous structures with controllable buckling geometrically and structurally behave much like plants' fruits. This replicates the biological morphologic change and elucidates the general mechanism and dynamics of the complex instability formation of heterogeneous 3D objects.

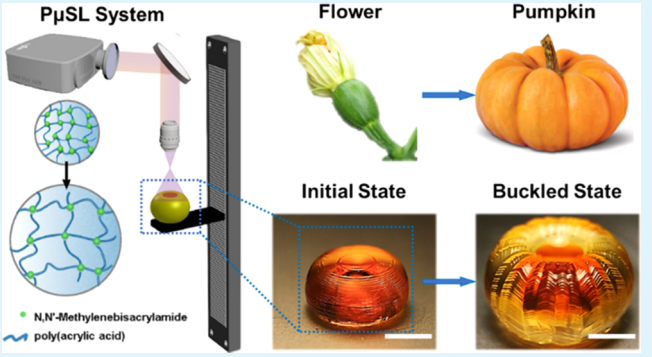

KEYWORDS: *morphogenesis, digital light processing (DLP), 4D printing, heterogeneous structure, instability, buckling*

1. INTRODUCTION

Different biological species differ from one another by their unique morphologies. While the embryonic development of each species or organ starts with a similar profile during growth, different morphologies eventually develop in their matured state. This biological process is termed morphogenesis. As part of the process, surface patterns and textures form across many length scales. For example, centimeter-scale cortical convolutions and groovy patterns on fruits,[1,2] millimeter-scale fingerprints,[3] and even micrometer-scale features on buckled tumor surfaces[4] and crumpled membranes of white blood cells.[5] The underlying mechanism of the morphology development, as a synergistic result of complicated biological, biochemical, and mechanical processes, is not yet fully understood.[6] Therefore, this unique yet common phenomenon is still of great importance and interest to biologists, materials engineers, and mechanics scientists. Understanding how different organisms evolve from similar, featureless immature states, usually embryos, into highly differentiated mature products would be meaningful for plant breeding in agricultural development and in the biomedical field for diagnosis and treatment.[5,7] Fundamentally, such three-dimensional (3D)-structure evolution processes would also aid the development of complex dynamic mechanical theories and shed light on the design of structural materials.

To understand the complex process of morphogenesis, extensive research and investigation have been conducted from the molecular, genetic, and cellular perspectives by biologists and botanists. Alternatively, other scientists take a macroscopic approach by studying the phenomena on the basis of mechanics and mathematics. The complicated biological tissue structures are usually abstracted into elastic or hyperelastic material models to study their fundamental stress and strain development.[2,8−13] Generally, different morphologies can be achieved via the formation of various surface patterns of mechanical instability during external loadings. The surface of the material would remain smooth until the applied compressive stress exceeds a critical value. Upon surpassing the threshold, buckling would occur on the surface of the material, characterized by the sudden localized deflection on the surface. To maintain a minimized free energy, undulation

Received: October 31, 2019
Accepted: November 19, 2019
Published: November 19, 2019

DOI: 10.1021/acsami.9b19730
ACS Appl. Mater. Interfaces XXXX, XXX, XXX−XXX

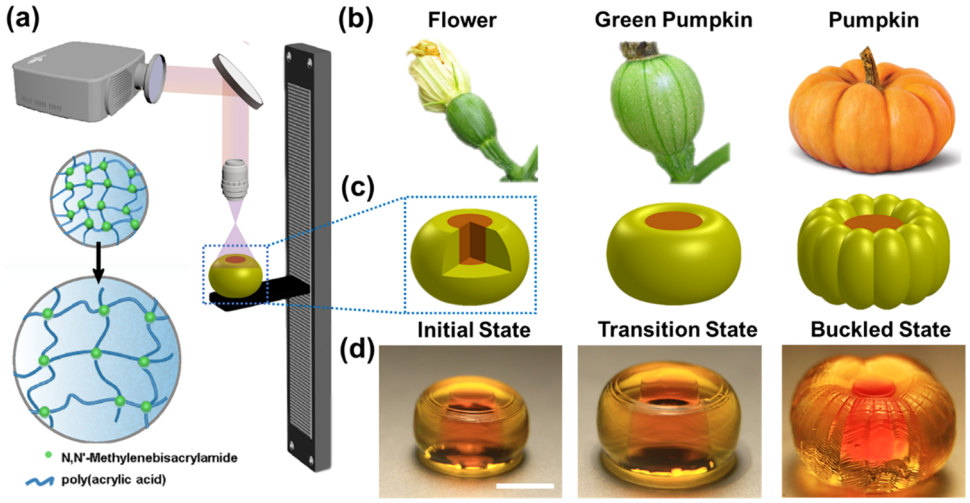

Figure 1. (a) Schematic of projection microstereolithography system, (b) growth of pumpkin, and (c) corresponding schematic diagram and (d) pictures of the printed hydrogel structure during the swelling process. The scale bar is 5 mm.

patterns will gradually develop across the surface of the material with the build-up of stress.

Based on the conventional instability theories, various theoretical calculations and finite element method (FEM) models have been developed to explain the formation of different morphologies during morphogenesis. Yinet al. have reported a quantitative mechanics framework of stress-driven anisotropic buckling on model spheroidal shell/core (film/substrate) systems. They approximated various natural fruits and vegetables as spheroidal stiff exocarp (shell)/compliant sarcocarp (core) systems, which exhibit intriguing buckling profiles.[2,14] Dervaux et al. have studied the circumferential deformation of a free hyperelastic disk mimicking the growth of green algae.[15] Jinet al. have investigated the crease formation of a soft tissue growing inside a rigid shell or outside a rigid core.[8]

To aid the theoretical development, active/responsive materials, which undergo volume and/or property changes in response to environmental stimulus, have been utilized for experimental validation of morphogenesis models. For example, Dervaux et al. utilized two different hydrogels with large distinction in swelling ratios to validate their model of shape transition in melanoma.[9] 3D printing technology has also been adopted for the facile fabrication of the material models. The combination of 3D printing and responsive materials is often referred to as four-dimensional (4D) printing, with time being the fourth dimension. 4D printing technology has been widely used to achieve various morphologies and intelligent behaviors. Shape-memory polymer fibers in elastomeric matrix were printed to be used as intelligent hinges to enable origami folding patterns such as box, pyramid, and airplanes.[16] Simple homogeneous tubular hydrogel structures with one end fixed have been fabricated by using digital light processing (DLP) 3D printing for the investigation of their buckling formation due to their instability.[17] Complex heterogeneous dual-gel bioinspired tubes were recently reported to achieve periodical buckling and intelligent behavior such as elongation and gripping.[18,19] Anisotropic hydrogel composites were reportedly applied in 4D printing of different biomimetic architectures, including a native orchid and a native calla lily flower.[20] In accordance to the prior 4D printed structures, anisotropy in the materials' stimuli-responsive behavior is essential to achieve programmable intelligent performance.[21]

Most studies of 4D printing focus on the transformation from one-dimensional (1D) rods or two-dimensional (2D) layered structures into 3D structures, while the time-dependent transformation starting from 3D structures is relatively less reported.[20,22,23] With the understanding that biological tissues are complex in both geometry and structure, we were inspired to take advantage of 4D printing fabrication to visualize and elucidate the morphogenetic mechanisms of various plants' organs. Essentially, we combined digital light processing (DLP)-based 3D printing technology with stimuli-responsive hydrogels to 4D print a heterogeneous core−shell dual-gel structure that geometrically and structurally imitates the pumpkin fruit. The material model mimics the growing process of pumpkins as the hydrogel swells and gradually develops pumpkin-like morphology. Thus, the 4D printed model can be used to monitor morphology evolution during its "growth" and shed light on the underlying morphogenesis mechanism. In the model, the less swellable, stiff core emulates the central part of the fruit, which consists of fibrous strands wrapping the seeds and two pole ends. The faster-swelling, soft shell mimics the soft mesocarp of the fruit where growth and volume expansion is most significant. The buckling wavelength, which determines the number of ridges and grooves on the "pumpkin" surface, can be readily tuned by controlling the expansion mismatch between the core and the shell. To the best of our knowledge, in this work, the time-dependent development of periodic buckling from the initiation site to the entire surface is studied for the first time. As a whole, this work elucidates the prerequisites, mechanisms, and the dynamic process of buckling on a 3D, heterogeneous, self-confined object without external boundary, resembling natural fruits geometrically. This is anticipated to contribute to the understanding of previously commonly studied buckling of uniform objects with boundary confinement.

2. EXPERIMENTAL SECTION

2.1. Materials. Acrylic acid (AAc), *N*,*N*′-methylene-bis-acrylamide (MBA), Sudan I dye, and Irgacure-819 (phenylbis(2,4,6-trimethylbenzoyl)phosphine oxide) were purchased from Sigma-Aldrich, Inc. Dimethyl sulfoxide (DMSO) solvent, ethanol, 0.05 M pH 7.00, dihydrogen potassium phosphate-sodium phosphate dibasic

DOI: 10.1021/acsami.9b19730
ACS Appl. Mater. Interfaces XXXX, XXX, XXX−XXX

buffer solution and 0.05 M pH 4.00 potassium biphthalate buffer solution, hydrochloric acid solution were purchased from Fisher Scientific Inc. All chemicals were used without further purification and treatment.

2.2. Preparation of Printing Precursor. To prepare the precursor solution for the 3D printing process, 24 wt % AAc as the monomer, 3.6 wt % MBA as the crosslinker, 0.6 wt % Sudan I dye as the photoabsorber, and 0.2 wt % Irgacure-819 as the photoinitiator were mixed in DMSO solvent. The mixture was vortexed and then ultrasound-treated for 10 min, producing a clear reddish precursor solution. This solution was used for printing all of the hydrogels described in this work. Additionally, ethanol was used to rinse the samples and a 0.05 M pH 7.00 dihydrogen potassium phosphate-sodium phosphate dibasic buffer solution was used as the swelling agent for the printed hydrogels for accurate control of the medium condition in all experiments.

2.3. Photolithography System. The printing was accomplished by a home-made, DLP-based 3D printing system, as shown in Figure 1a. The system was composed of a PRO4500 UV light (385 nm) projector from Wintech Digital System Technology Corporation, a motorized translation stage mounted to a motor controller, and other optical accessories from Thorlabs, Inc. The power density of the projected UV light is measured to be 2.0 mW/cm^2 by an ultraviolet light meter, Traceable Products. A home-made program was used to realize the coordination control of the projection and the movement of the stage. The resolution of the printer can achieve 30 μm on the $x-y$ plane and 10 μm in the z-axis direction.

2.4. Printing and Swelling Process. The printing process was carried out in air under ambient conditions. The printing precursor was cured by UV light layer by layer to print the 3D structure. A 3D CAD model was first designed and cut into a series of 2D patterns. The patterns were perpendicularly projected by the UV projector onto the stage, which was immersed in the precursor solution. To print a core−shell barrel structure, one large and one small concentric circles were projected sequentially for each layer. The larger circle was first projected for a short curing time of 3−4 s, followed by the projection of the small circle pattern for a longer curing time of 10 s in total to form the rigid core. Once a layer was printed, the support plate moved down allowing the projector to print another layer upon the top of the printed ones. For all of the samples with the core−shell structure, 50 layers were printed. The thickness of each layer was set to be 0.1 mm. Once the printing was completed, the as-printed hydrogel samples were rinsed in ethanol to remove the unreacted components and excess photoabsorber. Then, the clear hydrogel samples were immersed in a 0.05 M pH 7 buffer solution to swell, mimicking the growth process of pumpkins, as shown in Figure 1.

2.5. Measurement of Swelling Ratios and Rates. Thin discs of hydrogels of 2.1 cm diameter and 2 mm thickness were printed with various curing times to measure the swelling ratios of the printed hydrogels. As printed, the samples were first rinsed with ethanol to wash away the unreacted monomers and dyes. Then, they were put into pH 7 buffer solution to swell for 6 h. The changes in the discs' diameters over time were measured to calculate the linear swelling ratios, which were then cubed to obtain the volumetric swelling ratio of the hydrogels.

2.6. Measurement of Modulus. To measure Young's modulus of the printed hydrogels with different curing time, 15-layer samples in dog-bone shape were printed with various curing times (3−20 s per layer), rinsed with ethanol to get rid of unreacted monomers and extra dye, and then dried in an oven. Dynamic mechanical analysis (DMA850, TA Instruments) was used to measure the stress−strain curves of the printed samples. The moduli were obtained as the slope of the stress−strain curves.

2.7. Characterization of the Microstructures. A scanning electron microscope (SEM) was used to study the microstructures of the printed samples. The SEM images are obtained by using ZEISS Supra 40VP SEM. To prepare the samples for SEM imaging, the gels were first immersed in the buffer solution until they fully swelled. Then, they were frozen by using liquid nitrogen and left in the freeze dryer (Labconco Corporation, Freezone 1 L) overnight. A gold thin film was sputtered onto the samples for the SEM imaging, using the PELCOSC-7 auto sputter coater.

2.8. Simulation. The shape transition of hydrogels is a transient process, which mainly involves large deformation of the gel network and mass diffusion of water into/out of the gel. To model this complicated behavior, the inhomogeneous field theory that couples large deformation and mass diffusion was implemented in the environment of the commercial multiphysics modeling software COMSOL.[24,25] Details of the simulation methods can be found in the Supporting Information section.

3. RESULTS AND DISCUSSION

As the most versatile class of stimuli-responsive materials, hydrogels can undergo significant volumetric changes in response to various types of stimuli, such as pH, temperature, and humidity. Notably, the swelling ratio and mechanical performance of hydrogels can be easily tailored by tuning the chemical composition and the microstructure of the network. In this study, we 4D printed a poly(acrylic acid) (pAAc) hydrogel structure to serve as our material model. The hydrogel consists of crosslinked alkyl chains as the backbone and carboxyl groups extending outward from the backbone, thus driving its swelling in an environment of pH greater than the pK_a of the polymer (reported pK_a for acrylic acid is 4.3).

Figure 1a shows the schematic of the projection micro-stereolithography system used to print hydrogel structures in our work. The detailed printing procedures are described in Section 2. With this approach, we first printed a baby-pumpkin-like, heterogeneous hydrogel structure (henceforth referred to as "the pumpkin model") with coherent core and shell, as illustrated in the sectional figure in Figure 1c. The pumpkin model consists of a core cured for a longer time (10 s), marked in orange, and a circumferential shell cured for a shorter time (3.5 s), marked in green. This printing profile generates a highly swellable soft shell and a less swellable stiff core. Also, in the design, the core−shell radius ratio varies from 0.53 for the top and bottom layers at the two polar ends (pumpkin stem and base) to 0.4 at the equatorial layer throughout the total 50 layers of the entire model. It should be noted that since the pumpkin model is printed layer by layer, interlayer horizontal lines remain visible in both the as-printed state and swollen state of the pumpkin model in Figure 1d. These horizontal layered features are intrinsically different from the vertical circumferential ridges and grooves formed during the growth of the pumpkin model, and, therefore, neglected in our observation of the buckling. In the initial state, the surface of the pumpkin model is smooth, corresponding to the flowering stage of real pumpkins, as shown in Figure 1b. As the pumpkin model is triggered to swell in a pH 7 buffer solution, water starts to diffuse into the hydrogel networks and the pumpkin model will gradually swell. During this transition state, still no circumferential features are formed on the pumpkin model, which corresponds to the young, green pumpkin stage that takes place after the flower has withered. Eventually, the pumpkin model develops visible periodic ridges and grooves across the surface after 4 h of growth mediated by the buffer solution, as the shell buckles under the constraint of the core. The circumferential buckling features run continuously from one end of the pumpkin model to the other, corresponding to the mature stage in a pumpkin's life cycle. Through this process, the swelling evolution of the pumpkin model successfully mimics the morphogenesis of the pumpkin, starting from a featureless, barrel-like geometry and gradually

DOI: 10.1021/acsami.9b19730
ACS Appl. Mater. Interfaces XXXX, XXX, XXX−XXX

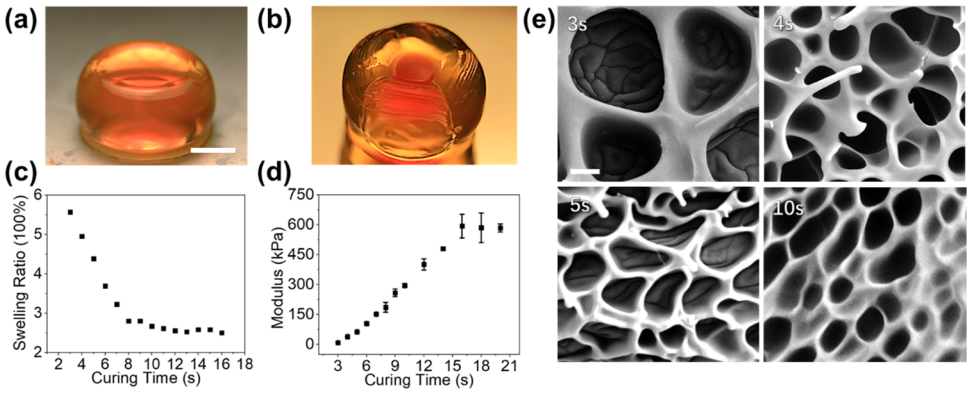

Figure 2. (a) 3 s cured homogeneous structure and (b) a heterogeneous pumpkin model with a 3 s cured shell and a 10 s cured core, (c) a plot of volumetric swelling ratio versus curing time and (d) a plot of modulus versus curing time of the homogeneous hydrogels, (e) SEM images of the microstructures in the hydrogels with different curing time (3, 4, 5, 10 s). The scale bars in (a, b) are 5 mm, and the scale bar in (e) is 5 μm.

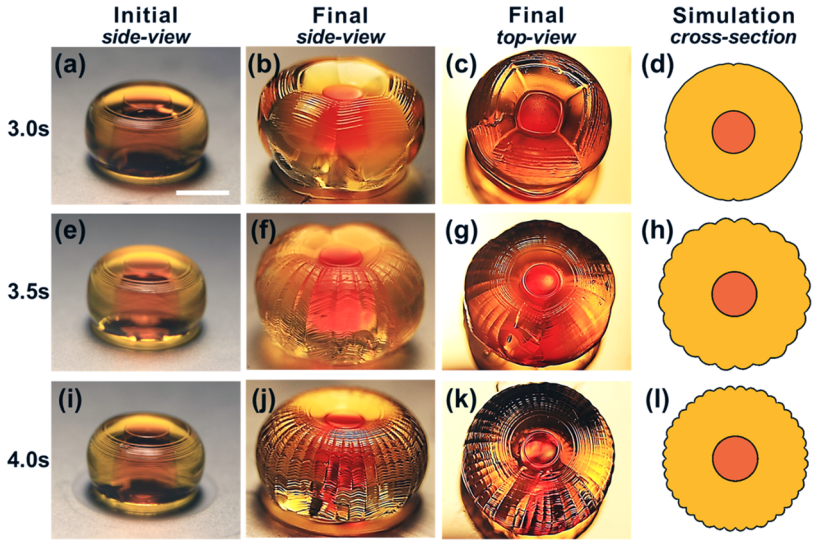

Figure 3. Initial state (a, e, i), final-state side view (b, f, j), and top view (c, g, k), simulated results (cross-section) (d, h, l) of the printed pumpkin models with different shell curing time: 3, 3.5, 4 s respectively. The scale bar is 5 mm.

developing into the final structure of periodic grooves and ridges.

To gain insight into the mechanism of the buckling formation, we first verified the role of the heterogeneity induced by the core−shell structure. A homogeneous control sample with no core−shell structure, fabricated with 3 s curing per layer, was compared side by side with the pumpkin model fabricated with a printing profile of 10 s curing for the core and 3 s curing for the shell in each layer, as shown in Figure 2a,b. The two samples were allowed to swell to comparable ratios in the same media. The homogeneous structure remained smooth, while circumferential buckling developed across the surface of the pumpkin model with heterogeneous structure after 4 h of swelling. This indicates that the imposed heterogeneity is crucial for the formation of periodic grooves and ridges on the material's surface. This heterogeneity enhances the strain mismatch between the superficial and in-depth part of the model, which helps to facilitate the buckling formation on the surface. Dimensional and mechanical ratios of heterogenous structures are commonly considered to govern the formation of buckling.[2,8] With our heterogeneous pumpkin model, we have further investigated the influence of three significant factors on the buckling formation: the mismatch of core/shell swelling and core/shell moduli as well as the ratio of core/shell radii.

We have verified that the modulus mismatch and self-imposed strain mismatch during swelling of the pumpkin model govern the formation of periodic buckling of its surface by systematic modulation of the material's properties. By tuning the curing time of each layer, materials fabricated with our system can exhibit drastically different moduli and swelling ratios using the same precursor, as shown in Figure 2c,d. For instance, the modulus for a hydrogel with 3 s curing time per layer is ∼9 kPa, while modulus for a 10 s sample is ∼295 kPa. Similarly, samples with a layer exposure time of 3 s led to an increase of 77% in diameter but only 38% for hydrogel with 10 s curing time per layer. The mechanical results were also supported by the microstructure analysis in Figure 2e. Layers with an exposure time of 3 s showed a pore size of about 20 μm, while 10 s exposure time produced a pore size of around 5 μm. Therefore, high dynamic ranges of modulus ratios and swelling ratios between the core and the shell could be realized by simple adjustment of the respective curing time of each part. Modulus mismatch of up to 70 folds and swelling ratio mismatch of up to 60% could be achieved in a single run of the printing process.

DOI: 10.1021/acsami.9b19730
ACS Appl. Mater. Interfaces XXXX, XXX, XXX−XXX

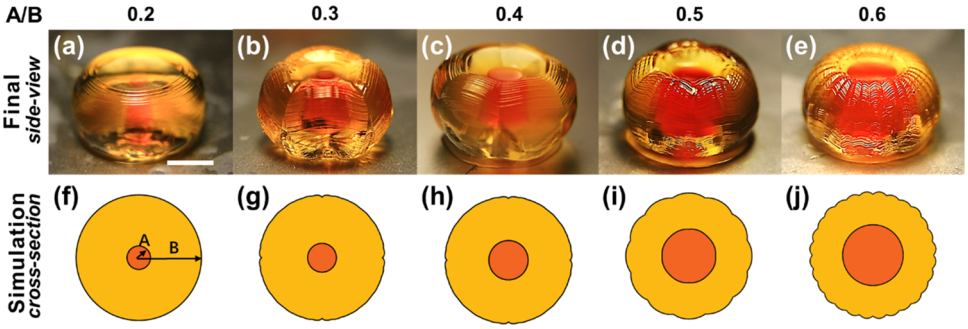

Figure 4. Printed pumpkin models of various core−shell radius ratios (A/B), all with 3 s cured shells and 10 s cured cores. The core−shell ratios are: (a) 0.2; (b) 0.3; (c) 0.4; (d) 0.5, and (e) 0.6. (f−j) Corresponding simulation results of the cross-section at the equatorial plane. The scale bar is 5 mm.

Based on the precise controllability and tunability of stiffness and swelling ratio, we fabricated a series of pumpkin models with different modulus mismatch and strain mismatch in the swollen state, as shown in Figure 3a−c,e−g,i−k. We used the same CAD pumpkin model with a fixed core−shell radius ratio of 0.4 on its equatorial plane for the printing. A constant curing time of 10 s for the core is set, while the curing time for the shell is varied from 3 to 3.5 s and 4 s, to create less swellable shells and, thus, decreasing core/shell modulus mismatch and strain mismatch. After 4 h of immersion in the pH 7 buffer solution, all three samples generated circumferential buckling extending from top to bottom and across the entire surface. The wavelength of the circumferential buckling decreases significantly with the decrease in modulus and strain mismatch. The number of ridges on the 3−10 s (shell curing time−core curing time) pumpkin model is ∼4, while for the 3.5−10 s pumpkin model, the number increased to ∼22, and for the 4−10 s model, the number further increased to ∼40. This is confirmed by finite element analysis of the cross-section at the equator of the pumpkin model, as shown in Figure 3d,h,l, where a similar trend of buckling formation is shown.

In the previous work reported by Yin et al., it is studied and discovered that the radius ratio between the core and the shell plays an important role in the morphogenesis, especially for the number of buckling and grooves.[2] Therefore, we printed a series of pumpkin models with the core/shell radius ratio varied (0.2−0.6) and the curing times fixed (3 s for the shell and 10 s for the core), to systematically study the influence of the radius ratio on the number of grooves. Here, the radius ratio value, A/B, is defined by the two concentric circles at the equatorial layer at their initial state. We denote "A" as the radius of the core, while "B" as the outer radius of the ring (shell), as shown in Figure 4f. The final-state morphologies of the series of 3−10 s pumpkin models with varying A/B from 0.2 to 0.6 are shown in Figure 4a−e. The wavelength of the circumferential buckling decreases with the increasing A/B. The number of ridges on a pumpkin model with A/B = 0.3 is ∼4 (Figure 4b), while for the 0.5 ratio pumpkin model the number increases to ∼6 with smaller ridges further forming on top of the 6 large ones (Figure 4d). As A/B increases to 0.6, the number of ridges increases to ∼30 (Figure 4e). This is also confirmed by a similar analysis of the cross-section at the equator of the pumpkin model, shown in Figure 4f−j. Details of the simulation can be found in the Section S1 of the Supporting Information.

To study the dynamic development process of periodic buckling across the surface, time-lapse observation was carried out throughout the swelling process of the pumpkin model. A sample was printed with a shell cured for 4 s and a core cured for 10 s to capture the onset and propagation of the ridge formation due to buckling. In the first 3.5 h of swelling, no buckling occurred on the surface. After being immersed in buffer solution for 3.5 h, faint buckling features start to form at the two ends of the pumpkin model, extending radially from the core to surrounding shell, as shown in Figure 5a. At this

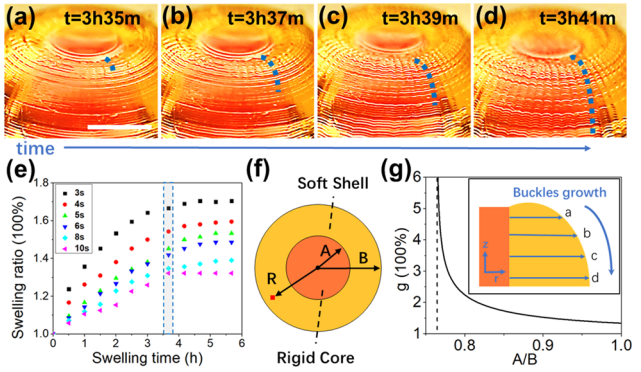

Figure 5. Buckles started to appear when the structure swelled to a critical level (a) and extended from the top to bottom (b, c) and eventually covered the surface of the structure (d), (e) the swelling ratios of hydrogels printed for different curing time (3−10 s) as the function of time, with the shaded region indicating the time period when buckling occurs, (f) the schematic of the equatorial layer of the pumpkin model, (g) the critical relative growth ratio, g, as a function of the core/shell radius ratio, A/B. Inset: schematic of the buckle growth, which starts from the top to equatorial plane, corresponding to (a−d). The scale bar is 5 mm.

stage, only the top few layers show buckling features and the rest of the surface remained smooth. The sudden formation of buckling features is attributed to the "snap through" aspect of buckling. Previously, Jin et al. have reported an analytical study of a tubular, soft shell growing outside of a rigid core.[8] Based on their theory, here we further concluded the critical condition for the onset of circumferential buckling on the outer surface of the shell in our pumpkin model with both the core and the shell swelling, which is given as

$$g^3/\left(\left(\frac{A}{B}\right)^2 - g^3\left(\left(\frac{A}{B}\right)^2 - 1\right)\right) = 2.4$$

where g is the relative growth ratio, which is defined as $g = g_{shell}/g_{core}$, and A and B are the same radii as we have defined

DOI: 10.1021/acsami.9b19730
ACS Appl. Mater. Interfaces XXXX, XXX, XXX−XXX

above. The detailed calculation is described in the Supporting Information, Section S3. This equation is based on the several assumptions: (1) the deformation of the hydrogel is taken as elastic and incompressible, which means that for a constant curing time, the growth ratio (swelling ratio) will be the same; (2) both the core and the shell grow homogeneously, so the growth ratio in the radial, circumferential, and longitudinal directions of the shell has the same value, $g_r = g_\theta = g_z$; (3) it is assumed that there is no deformation in the z-direction. Thus, the critical relative growth ratio (i.e., the threshold for buckling initiation), g, as a function of A/B can be plotted as Figure 5g. For a given A/B, the relative growth ratio needs to exceed a threshold for the buckling to occur, which is similarly observed in our experimental results.

At ∼3.5 h, the core has been fully swelled while the shell is still growing. The buckling formation and development occurred within the gray region in Figure 5e. Within a short period of time afterward, the circumferential buckling ridges extend from the poles to the equator and eventually cover the entire surface of the pumpkin model, as progressively shown in Figure 5b−d. The length of formed ridges is marked with blue dashed lines for better illustration. This spatial and temporal evolution of the circumferential buckling patterns pose special interest for study. The reason why the buckling onset in the polar region is faster than the equator region can also be explained using the above equation. With a large A/B value, the critical relative growth ratio is more readily achieved. Since the polar region has larger A/B (A/B = 5.3:10) than the equatorial region (A/B = 4:10), instability will first occur in the polar region. As the structure continues to swell, the regions away from the poles consecutively reach the critical condition for the onset of buckling, leading to the propagation of ridges extending from the two poles to the equator with the evolution of time, as illustrated in the inset of Figure 5f. However, the theoretical calculation predicts that the numbers of ridges formed should change with different core−shell ratios, whereas for our pumpkin model with various core−shell ratios along the z-axis, the number of ridges remains the same in every layer. This may result from the strong interaction between each layer as they are coherently jointed at each interface, thus additional strain energy would arise if different layers assume different numbers of ridges. Therefore, as the buckling occurs in previous layers along the propagation path, it will induce the subsequent layer to buckle in the same radial position to mitigate the excess interlayer strain energy. As a result, the printed layers with varying core−shell ratios synergistically display a single mode of buckling, where the buckling pattern runs continuously between the two poles.

As shown in Figure 5f, it is predicted by the equation that the buckling occurred only if A/B is larger than $\sqrt{7/12}$, while in the experimental results it shows a lower threshold of A/B for buckling formation. This can be attributed to the much more complex conditions of the experimental results. Due to the layer-by-layer additive manufacturing method, the growth of hydrogel structures, in practice, was not homogeneous in longitudinal and lateral directions. Besides, it was assumed that there was no deformation in *the* z-direction, for the convenience of calculation. Other factors such as the model's height and the curvature of the shell have not been considered. Since a number of assumptions have been made to simplify the conditions in the analysis, challenges to fully understand the mechanism behind the buckling formation still remain and more investigation is under way. A primary exploration has been conducted by tuning the deformation gradient in the z-direction, λ_z. If $\lambda_z < 1$, it can describe a condition that a compressive stress is applied at the two poles of the model to force it to shrink in the z-direction. As shown in Figure S4, such a compression will eventually lead to a lower threshold of A/B for buckling initiation as well as a lower critical relative growth ratio, which is much consistent with the experimental results. Although the pumpkin model in the present experiment did not shrink in the z-direction, this analytical result confirms the significant influence of the constrain from the polar ends. In addition, wrinkling of pressurized elastic shells, which are similar periodical buckling of our model, has also been reported.[26] As far as it goes, the buckling formation of the pumpkin model is attributed to the mismatch between the core and the shell in swelling ratio and modulus as well as the constraint boundary at the two ends. As long as the critical conditions of buckling formation are met, circumferential buckling can also form on the surface of a printed pumpkin model with a hollow core as shown in Figure S5, which more closely resembles the structure of a real pumpkin.

Apart from mimicking the morphogenesis of the Cucurbita species like pumpkins, we have also applied our platform to mimic the morphogenesis of other fruits and vegetations.[27−31] For example, the curvy edges of cabbage, bent flower petals, and twisted bean shells. To mimic cabbages, we printed a core−shell heterostructured thin disc out of the same hydrogel materials, as shown in Figure 6a. The swelling (strain) mismatch between the 3 s cured soft shell and the 10 s cured hard core, after 2 min of swelling in buffer solution, led to the formation of the cabbage-leaf-like wavy morphology, as shown in Figure 6b. For mimicking flower petals, we printed a double-layer heterostructure, as shown in Figure 6e. The difference in swelling ratios between the two layers in response to water allows the petals to act as a bilayer actuator bending to the center, which mimics the morphology of chrysanthemum. Besides core−shell structures and bilayer structures, distinct plant morphologies can also be controllably formed by placing

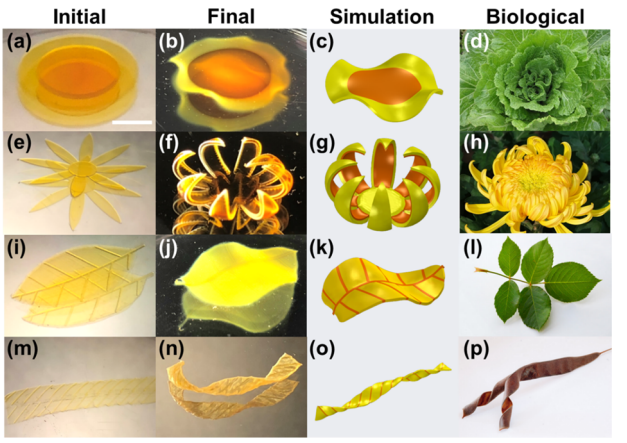

Figure 6. Morphologic transformation of different printed biomimetic structures: the initial plain structures (a, e, i, m) were printed and rinsed with ethanol, then immersed in water to allow them to develop into their final states (b, f, j, n). The simulated models (c, g, k, o) and the images of real cabbage flowers/leaves (d), chrysanthemum (h), leaves of rose (l), and helix strips of Bauhinia pods (p) indicate the corresponding emulation of their 3D geometrical morphologies evolved from the predesigned 2D heterogeneous structures. The scale bar is 5 mm.

DOI: 10.1021/acsami.9b19730
ACS Appl. Mater. Interfaces XXXX, XXX, XXX−XXX

stiff lines in a soft film. In Figure 6i, we printed a leaf-shape structure with a soft mesophyll and a stiff vein inside. After immersion in buffer solution for 2 min, the printed leaf will turn into a curved profile, as shown in Figure 6j. In addition, a soft strip with 45 degree oriented, stiff slash lines embedded was printed and developed into a helix structure similar to Bauhinia pods, as shown in Figure 6m,n. Details of the printing process can be found in the Supporting Information (Figure S6). The simulations of the four different structures shown in Figure 6c,g,k,o show equivalent results as the experimental ones, which closely resembled the natural organisms, as shown in Figure 6d,h,l,p. This further verified the geometry evolution of the 4D printing designs and processes. By designing heterogeneous structures with tunable modulus mismatch and swelling mismatch, we can controllably fabricate heterogeneous structures to mimic the morphogenesis and reproduce the morphologies of various plants.

4. CONCLUSIONS

In summary, by 4D printing a heterostructured material that structurally and geometrically represents pumpkins, we have successfully mimicked the morphogenesis of pumpkins, a complex spatiotemporal evolution that starts from a featureless, barrel-like geometry and gradually develops into a final structure with periodic grooves and ridges. We have evaluated the importance of heterogeneity in morphogenesis with our model. Furthermore, we have explored the governing parameters of the produced patterns by taking advantage of 4D printing, which allowed for achieving a large range of modulus mismatch and strain mismatch as well as tunable core/shell radius ratios. Assumptions have been utilized to understand the mechanism of the buckling formation in a simplified way. The present differences between experimental results and analytical calculation indicate that challenges still remain, and the further investigation is under way. We have also demonstrated that the platform could be used for mimicking the morphogenesis of a wide selection of plants. The swelling process of our printed models presents a synthetic morphogenesis, which can help shed light on the mechanism behind the practical morphological formation of natural plants and extend the understanding of complex mechanics of heterogeneous high-dimensional dynamic architectures. The knowledge may open a new access to the design and fabrication of previously unachievable complex 3D architectures. It can facilitate the studies and control of the biological tissues and organs. The printable biocompatible hydrogels with intellectual behaviors are anticipated to benefit broad agricultural, soft robotics, and additive manufacturing fields.

ASSOCIATED CONTENT

Supporting Information

The Supporting Information is available free of charge at https://pubs.acs.org/doi/10.1021/acsami.9b19730.

Simulation detail; analytical calculation procedure; additional experimental results; printing patterns of different biomimetic structures (PDF)

AUTHOR INFORMATION

Corresponding Author

*E-mail: ximinhe@ucla.edu (X.H.).

ORCID

Hanqing Jiang: 0000-0002-1947-4420

Ximin He: 0000-0001-8845-4637

Author Contributions

[§]D.W. and J.S. contributed equally.

Notes

The authors declare no competing financial interest.

ACKNOWLEDGMENTS

The authors thank the support of the ONR award N000141712117, the ONR award N00014-18-1-2314, the AFOSR award FA9550-17-1-0311, the AFOSR award FA9550-18-1-0449, the Hellman Fellows Funds, and the start-up funds from the University of California, Los Angeles.

REFERENCES

(1) Liu, Y.; Yang, X.; Cao, Y.; Wang, Z.; Chen, B.; Zhang, J.; Zhang, H. Dehydration of Core/Shell Fruits. *Comput. Graph.* **2015**, *47*, 68−77.

(2) Yin, J.; Cao, Z.; Li, C.; Sheinman, I.; Chen, X. Stress-Driven Buckling Patterns in Spheroidal Core/Shell Structures. *Proc. Natl. Acad. Sci. U.S.A.* **2008**, *105*, 19132−19135.

(3) Yin, J.; Gerling, G. J.; Chen, X. Mechanical Modeling of a Wrinkled Fingertip Immersed in Water. *Acta Biomater.* **2010**, *6*, 1487−1496.

(4) Ciarletta, P. Buckling Instability in Growing Tumor Spheroids. *Phys. Rev. Lett.* **2013**, *110*, No. 158102.

(5) Wang, L.; Castro, C. E.; Boyce, M. C. Growth Strain-Induced Wrinkled Membrane Morphology of White Blood Cells. *Soft Matter* **2011**, *7*, 11319.

(6) Mirabet, V.; Das, P.; Boudaoud, A.; Hamant, O. The Role of Mechanical Forces in Plant Morphogenesis. *Annu. Rev. Plant Biol.* **2011**, *62*, 365−385.

(7) Phillips, G. C. In Vitro Morphogenesis in Plants-Recent Advances. *In Vitro Cell. Dev. Biol.: Plant* **2004**, *40*, 342−345.

(8) Jin, L.; Cai, S.; Suo, Z. Creases in Soft Tissues Generated by Growth. *Europhys. Lett.* **2011**, *95*, No. 64002.

(9) Dervaux, J.; Couder, Y.; Guedeau-Boudeville, M. A.; Ben Amar, M. Shape Transition in Artificial Tumors: From Smooth Buckles to Singular Creases. *Phys. Rev. Lett.* **2011**, *107*, No. 018103.

(10) Armon, S.; Efrati, E.; Kupferman, R.; Sharon, E. Geometry and Mechanics in the Opening of Chiral Seed Pods. *Science* **2011**, *333*, 1726−1730.

(11) Savin, T.; Kurpios, N. A.; Shyer, A. E.; Florescu, P.; Liang, H.; Mahadevan, L.; Tabin, C. J. On the Growth and Form of the Gut. *Nature* **2011**, *476*, 57−62.

(12) Li, B.; Cao, Y.-P.; Feng, X.-Q.; Gao, H. Surface Wrinkling of Mucosa Induced by Volumetric Growth: Theory, Simulation and Experiment. *J. Mech. Phys. Solids* **2011**, *59*, 758−774.

(13) Li, B.; Jia, F.; Cao, Y. P.; Feng, X. Q.; Gao, H. Surface Wrinkling Patterns on a Core-Shell Soft Sphere. *Phys. Rev. Lett.* **2011**, *106*, No. 234301.

(14) Yin, J.; Chen, X.; Sheinman, I. Anisotropic Buckling Patterns in Spheroidal Film/Substrate Systems and Their Implications in Some Natural and Biological Systems. *J. Mech. Phys. Solids* **2009**, *57*, 1470−1484.

(15) Dervaux, J.; Ben Amar, M. Morphogenesis of Growing Soft Tissues. *Phys. Rev. Lett.* **2008**, *101*, No. 068101.

(16) Ge, Q.; Dunn, C. K.; Qi, H. J.; Dunn, M. L. Active Origami by 4d Printing. *Smart Mater. Struct.* **2014**, *23*, No. 094007.

(17) Lee, H.; Fang, N. X. Micro 3d Printing Using a Digital Projector and Its Application in the Study of Soft Materials Mechanics. *J. Vis. Exp.* **2012**, No. e4457.

(18) Liu, J.; Liu, W.; Pantula, A.; Wang, Z.; Gracias, D. H.; Nguyen, T. D. Periodic Buckling of Soft 3d Printed Bioinspired Tubes. *Extreme Mech. Lett.* **2019**, *30*, No. 100514.

DOI: 10.1021/acsami.9b19730
ACS Appl. Mater. Interfaces XXXX, XXX, XXX−XXX

(19) Liu, J.; Erol, O.; Pantula, A.; Liu, W.; Jiang, Z.; Kobayashi, K.; Chatterjee, D.; Hibino, N.; Romer, L. H.; Kang, S. H.; Nguyen, T. D.; Gracias, D. H. Dual-Gel 4d Printing of Bioinspired Tubes. *ACS Appl. Mater. Interfaces* **2019**, *11*, 8492−8498.
(20) Gladman, A. S.; Matsumoto, E. A.; Nuzzo, R. G.; Mahadevan, L.; Lewis, J. A. Biomimetic 4d Printing. *Nat. Mater.* **2016**, *15*, 413−418.
(21) Erol, O.; Pantula, A.; Liu, W.; Gracias, D. H. Transformer Hydrogels: A Review. *Adv. Mater. Technol.* **2019**, *4*, No. 1900043.
(22) Ding, Z.; Weeger, O.; Qi, H. J.; Dunn, M. L. 4d Rods: 3d Structures Via Programmable 1d Composite Rods. *Mater. Des.* **2018**, *137*, 256−265.
(23) Kuang, X.; Roach, D. J.; Wu, J.; Hamel, C. M.; Ding, Z.; Wang, T.; Dunn, M. L.; Qi, H. J. Advances in 4d Printing Materials and Applications. *Adv. Funct. Mater.* **2019**, *29*, No. 1805290.
(24) Hong, W.; Zhao, X.; Zhou, J.; Suo, Z. A Theory of Coupled Diffusion and Large Deformation in Polymeric Gels. *J. Mech. Phys. Solids* **2008**, *56*, 1779−1793.
(25) Wang, X.; Zhai, Z.; Chen, Y.; Jiang, H. A Facile, Robust and Versatile Finite Element Implementation to Study the Time-Dependent Behaviors of Responsive Gels. *Extreme Mech. Lett.* **2018**, *22*, 89−97.
(26) Vella, D.; Ajdari, A.; Vaziri, A.; Boudaoud, A. Wrinkling of Pressurized Elastic Shells. *Phys. Rev. Lett.* **2011**, *107*, No. 174301.
(27) Liu, Z.; Swaddiwudhipong, S.; Hong, W. Pattern Formation in Plants Via Instability Theory of Hydrogels. *Soft Matter* **2013**, *9*, 577−587.
(28) Forterre, Y.; Dumais, J. Materials Science. Generating Helices in Nature. *Science* **2011**, *333*, 1715−1716.
(29) Stoychev, G.; Puretskiy, N.; Ionov, L. Self-Folding All-Polymer Thermoresponsive Microcapsules. *Soft Matter* **2011**, *7*, 3277.
(30) Wu, Z. L.; Moshe, M.; Greener, J.; Therien-Aubin, H.; Nie, Z.; Sharon, E.; Kumacheva, E. Three-Dimensional Shape Transformations of Hydrogel Sheets Induced by Small-Scale Modulation of Internal Stresses. *Nat. Commun.* **2013**, *4*, No. 1586.
(31) Li, B.; Cao, Y.-P.; Feng, X.-Q.; Gao, H. Mechanics of Morphological Instabilities and Surface Wrinkling in Soft Materials: A Review. *Soft Matter* **2012**, *8*, 5728.

DOI: 10.1021/acsami.9b19730
ACS Appl. Mater. Interfaces XXXX, XXX, XXX−XXX